Rated and overload capability of a synchronous PM spoke motor for e-bike application

Chiara Contò and Nicola Bianchi
Dept. of Ind. Engineering
University of Padova
Padova, Italy

***Abstract*—The electric bicycle industry is experiencing a rapid transformation, becoming increasingly popular as a form of urban transportation. This study presents the analysis of a typical electric motor configuration used in such application. The focus is on the nominal and overload capability, evaluated through both finite element simulations and experimental tests. Motor nominal and overload capabilities are examined. Thermal behaviour is determined through thermal test and a thermal network. Maximum torque ans power delivered, maximum speed achievable and possible ground tilt that can be overcame are calculated. Finally, an esteem of the efficiency during nominal and overload operation is carried out, based on losses computation.**

***Index Terms*—Permanent Magnet Synchronous Motor (PMSM), Synchronous Machine (SM), Change of polarity, Motor design**

I. Introduction

Electric Propelled Micro-Mobility Devices, specifically electric bicycles (e-bikes), have emerged as a prevailing trend projected to witness exponential growth in the forthcoming decades. E-bikes are bicycles integrated with an electric motor that boosts the rider's power output through a specific electrical power input.

Regulated by EU standards, the electric assistance provided by e-bikes is limited to a maximum speed of 25 $\mathrm{km/h}$ and a maximum power output of 250 W. Even though the continuous power of the motor is limited, the motor drive is designed to exhibit temporary power that is much higher. Typically, a low-voltage lithium-ion battery with a DC bus voltage of 36 V (though increasingly 48 V batteries are gaining popularity) powers the e-bikes.

Focusing on electric motor typology, literature primarily concerns brushless DC electric motors [1], [2]. However, the current state-of-the-art has gravitated towards the implementation of synchronous Permanent Magnet (PM) motors, particularly for high-power traction applications. Research on electric motor design for e-bike application can be found throughout the literature.

One notable study regards an in-hub PM-assisted synchronous reluctance motor with outer rotor [3]. Compared to commercial brushless DC motors, this design exhibits a 28% increase in torque density, a 50% reduction in cogging torque and an 8% reduction in torque ripple. Moreover, this design reduces PM usage and associated costs by 40%. However, the efficiency of this design is relatively lower due to the significantly smaller volume of PMs utilized.

Another topic of research explores the utilization of switched reluctance technology in e-bike applications. An example is presented in [4], where the study examines the external rotor structure of an in-wheel e-bike motor, enabling its integration into the wheel hub. Additionally, a study in [5] presents an optimized design of a switched reluctance motor, aiming to achieve performance parameters and dimensional constraints comparable to those of a commercial PM e-bike motor.

Despite the cost-effectiveness and durability offered by switched reluctance motors, they suffer from high torque ripple and noise, prompting a focus shift to PM synchronous motor topology in this research. PM synchronous motors have gained popularity in light EV applications due to their ability to overcome some of the limitations present in reluctance machines. These machines are particularly well-suited for high-performance applications that require high torque density, especially at low speeds, making them an ideal fit for the evolving demand of e-bike application.

This study undertakes a thorough examination of a typical e-bike electric motor configuration, presenting both Finite Element (FE) simulations and experimental test results. The motor considered is a synchronous motor with interior PMs. The stator is characterized by a fractional-slot winding with non-overlapped coils, adhering to common practices in the majority of light EV applications. The novelty of this study lies in its results, regarding an extensive investigation of the capabilities of PM synchronous motors for e-bikes. Alongside the analysis of the motor's nominal operation, this study also delves into its overload operation, providing a comprehensive analysis of the operational boundaries of a typical motor for this application.

The paper is outlined as follows. Section II introduces the fractional-slot PM motor, specifying its advantages and drawbacks. Subsequently, a magneto-static finite element simulation is carried out on a 14-slots / 10-poles motor and experimental measures are compared to such results. Section III presents a comparative study of simulation and experimental results, thoroughly investigating the motor's behaviour under no-load, nominal, and overload conditions. Furthermore, the thermal behaviour of the machine is analysed, and a thermal

Fig. 1: Rotor detail of the PM motor under analysis.

Parameter	Symbol	Value	Unit
External stator diameter	D_e	80	mm
Inner stator diameter	D_s	47	mm
Air gap	g	0.5	mm
Stator slots	Q_s	12	-
PM thickness	t_m	3	mm
PM length	l_m	9	mm
Stack length	L_{stk}	20	mm

TABLE I: Motor geometry parameters.

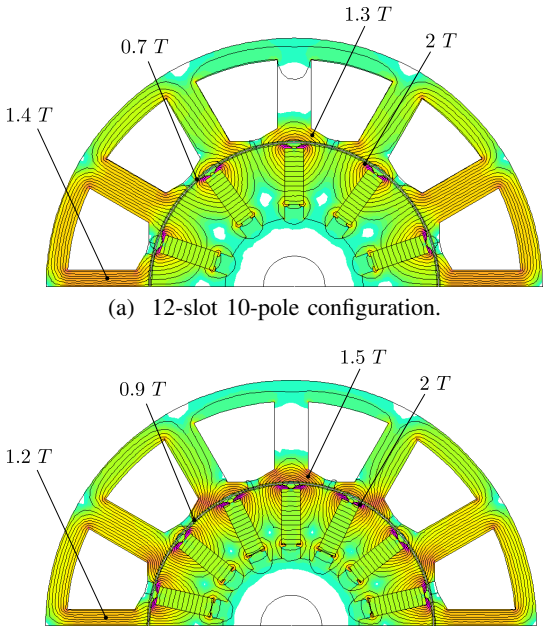

(a) 12-slot 10-pole configuration.

(b) 12-slot 14-pole configuration.

Fig. 2: No-load flux lines and flux density map of $12/10$ and $12/14$ motors.

network of the studied motor is constructed using thermal measures. Finally, Section IV focuses on losses estimation via FE simulation, particularly on rotor losses due to magneto-motive force sub- and higher harmonics. Conclusions are presented in Section V.

II. Motor configuration

A. 12/14 motor geometry

In light electric vehicle applications, fractional-slot windings with non-overlapped coils are commonly used [6]. These windings are suitable for high-pole machines and have reduced end-winding lengths, resulting in lower copper weight and Joule losses. Therefore, such configuration is suitable for e-bike application, having high torque density and efficient thermal dissipation. However, some designs may experience low winding factor or Magneto Motive Forces (MMF) sub-harmonics, leading to additional rotor losses and torque ripple. In an e-bike application, the electric motor's ability to handle overloads is important. The fractional-slot motor configuration is ideal for this purpose, as it has low Joule losses and efficient thermal dissipation.

Fig. 1 shows the rotor of the machine considered, while TABLE I summarizes its main geometry parameters. It is a fractional-slot synchronous PM motor with 12 slots and 14 poles, that is a common configuration among existing e-bike commercial motors. The rotor has interior PMs with a spoke-type disposition. In the following it will be referred to as $12/14$ motor.

B. Comparison to 12/10 configuration

The $12/14$ motor configuration presented is compared to the $12/10$ one, having the same machine geometry except for the number of poles. As shown in Fig. 2, flux-density is different. A higher flux-density is reached in teeth iron for the low number of poles machine (Fig. 2a), while a higher air gap flux-density is reached by the high number of poles machine (Fig. 2b). Consequently, a lower torque is expected from the $12/10$ configuration, having same dimensions of the $12/14$ configuration, but a lower number of poles. From Fig. 2 the radial balanced forces and the machine periodicity (equal to two) can be observed.

The MMF of both configurations is computed, considering a unitary current loading. The waveform is the same for both configurations, but the harmonic content is different. Fig. 3b shows the main harmonic together with sub harmonics and higher harmonics (up to the 50^{th}) of both configurations. The main harmonic order correspond to the number of pole pairs of the configuration, meaning that the $12/14$ MMF is characterized by sub harmonics of 1^{st} and 5^{th} order, while the $12/10$ MMF has only the 1^{st} sub harmonic. Such sub harmonics cause additional losses, increase heating and produce vibrations. In particular, the $12/14$ sub harmonic of 5^{th} order is higher than the fundamental, thus it can produce high losses.

Fig. 4 shows the torque comparison, both in no-load and on-load conditions. The rotor position changes from 0° to 30°, i. e. a slot angle. The torque values are per unit, considering the $12/10$ waveform peak as base value of the cogging torque (Fig. 4a) and the $12/10$ average value as base of the on-load torque (Fig. 4b). As shown in Fig. 4a, the cogging torque of the $12/14$ configuration is almost half the $12/10$ one. Fig. 4a shows the torque when both motors have the same current density. The $12/14$ configuration exhibits a torque 25 % higher than the $12/10$ torque and a torque ripple of 5 %, versus the 8

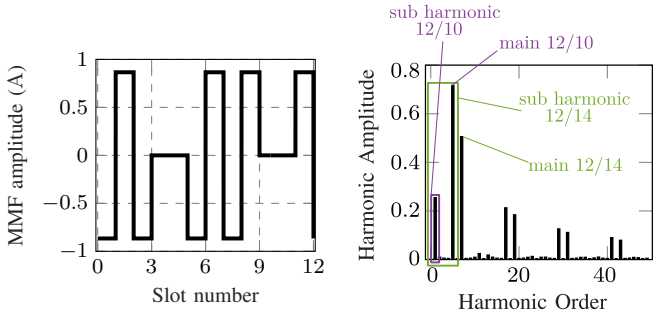

(a) Waveform. (b) Harmonics.

Fig. 3: MMF comparison of the 12/10 and 12/14 configurations.

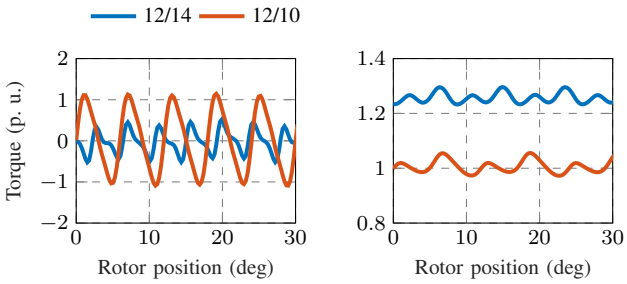

(a) Cogging torque. (b) On-load torque.

Fig. 4: No-load and on load torque versus rotor position, comparison between 12/14 and 12/10 motor configurations.

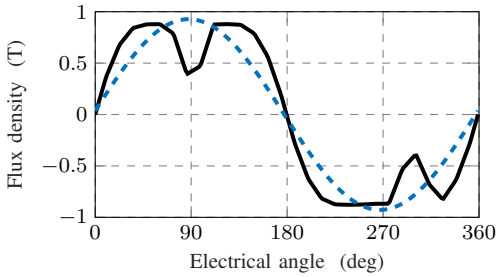

Fig. 5: No-load air gap flux-density versus angular position (solid line) and first harmonic (dashed line).

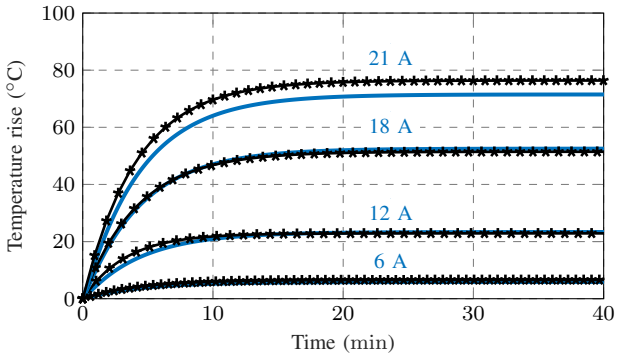

Fig. 6: Thermal test for different currents supplied, experimental (solid black lines with asterisk) and simulation results (solid blue lines).

% of the 12/10 motor. The higher torque is due to the higher PM volume (same PM dimensions but 4 additional poles), while the lower torque ripple is related to the lower cogging torque oscillation.

III. Motor Capability

In this Section motor capabilities are defined through both simulations and experimental tests. Two-dimensional magneto-static finite element analysis is carried out by means of *femm* 4.2 simulation software [7]. The minimum portion of the machine is modelled (i.e. half motor), imposing anti-periodic boundary conditions to its edges.

A. No-load simulation results

First, no-load magneto-static simulations are carried out to identified maximum iron flux-density values and air gap flux-density waveform. Fig. 2a shows no-load flux lines and flux density map, highlighting the air gap flux density of 0.9 T, the tooth maximum flux density of 1.2 T and some regions where saturation occurs. Fig. 5 displays the air gap flux density waveform, characterized by a fundamental harmonic of 0.84 T.

B. Thermal measurement

At first the rated and overload current values are identified through a thermal test. Fig. 6 shows the winding temperature rise in time when different currents are supplied (dotted black lines). Allowing a maximum temperature rise of about 50 °C, the 18 A current is the limit value. The current density associated to such a current is 11 $\mathrm{A/mm^2}$, that is a high value for a nominal supplying condition. However, such motor is characterized by a good heat dissipation, due to the non-overlapped coils winding and to the finned case.

In order to model the motor thermal behaviour, a thermal network is built. Thermal resistances are computed for copper wires in slot, insulation in slot, teeth, back-iron, motor case and contact air (very thin air volume between the stator and the case). Thermal capacitances are defined for the copper winding, teeth and back-iron, and the case. In Fig. 6 simulation results (solid blue lines) are compared to experimental tests (dotted black lines). The thermal network developed is verified for currents up to 21 A, predicting very precisely the steady-state temperature rise and the thermal dynamic.

The temperature rise when higher currents are supplied is computed only through thermal network. Fig. 7 shows the absolute winding temperature evolution esteemed through the thermal network developed. The environmental temperature considered is 24 °C. The temperature reached when the rated current is supplied equals 75 °C. With 21 A the d steady-state temperature is 95 °C, with 24 A it is 118 °C and with 30 A it reaches about 170 °C.

PMs are Samarium Cobalt magnets, which are very robust against demagnetization even at high temperatures. However, the winding temperature is limited to values lower than 120 °C. Thus, the overload supply condition deduced from the thermal test is characterized by a current of 24 A (15 $\mathrm{A/mm^2}$).

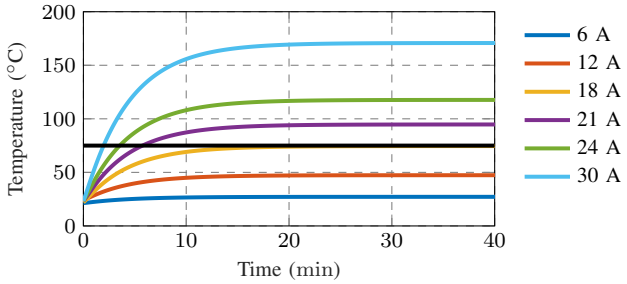

Fig. 7: Temperature evolution for different currents supplied, simulation results.

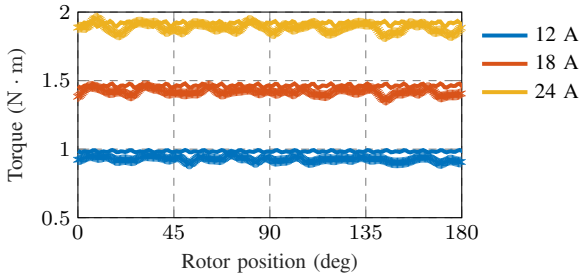

Fig. 8: Torque versus position, simulation (solid line) and experimental (dotted line) results.

Higher currents yields higher winding temperatures, thus they can be sustained for a limited time. Considering the predicted temperature evolution, the 24 A overload current can be sustained for 4 min.

C. On-load capabilities

Fig. 8 displays the torque measured when the rotor completes a rotation of 180 mechanical degrees. TABLE II compares simulation and experimental results, showing that the average torque value is very similar, while the oscillation is slightly lower in experimental tests. The temperature reached by the stator winding is specified, both simulated and from experimental test (when measured).

The operating region in the torque-speed plane can be computed from measures. The torque remains constant up to the base speed, then the demagnetizing current is increased, weakening the PM flux. The torque delivered decreases, while the speed increases. Fig. 9 shows the torque and power versus speed characteristics. The rated speed is about 2200 rpm, while the maximum speed can reach 16000 rpm during overload operation. During nominal operation the peak power delivered is equal to 290 W, while it reaches 390 W during overload operation.

	Current (A)	Torque (N m)	Ripple (%)	Temperature (°C)
measured	12	0.98	11	47
simulated		1	2	47.4
measured	18	1.49	7	73.5
simulated		1.47	2	74.5
measured	24	1.92	8	-
simulated		1.89	2	118

TABLE II: Torque comparison.

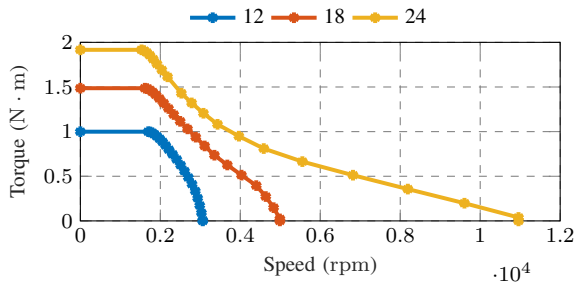

(a) Torque versus speed.

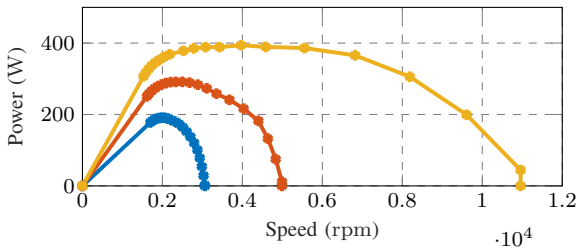

(b) Power versus speed.

Fig. 9: Torque and power versus speed for different current amplitudes, experimental results.

Fig. 10a shows the torque versus speed capability of the electric motor together with the load diagram, human muscular torque not included. Considering resistance forces of a bike moving uphill (Fig. 10b), the power consumed to drive the bike is due to overcoming wind resistance F_{drag}, lifting mass up hills F_{hill} and to overcoming frictions $F_{friction}$. Load diagrams are computed for different ground slopes α and speeds as in [1]. An alternative approach is described in [8]. The gear transmission ratio (from electric motor to the wheel) is $1:35$ and a total mass of e-bike and rider equal to 90 kg is considered.

With just the electric motor contribution to the wheel, a maximum torque of 70 $\mathrm{N}\cdot\mathrm{m}$ can be delivered to the wheels, reaching a maximum speed of 420 rpm. The rider-bicycle system can overcome a tilt of 2.8 degrees (5 % slope) during nominal operation, 6.4 degrees (11 % slope) during overload operation without any muscular contribution.

D. Drive cycle

In order to extensively describe the motor capabilities, a realistic drive cycle is defined and the motor tested. The drive cycle is 2 hours and 7 minutes long, with a route that can be divided into 13 different stages. It starts with a flat road, followed by a gentle uphill, and a smooth downhill. Then, a high slope steep ascent leads to a short descent. Afterward, a long and flat stretch allows for a long smooth driving. Then, a slight incline before a straightforward downhill. The route returns to a smooth and level road before another descent. The drive ends with a flat stage, a smooth descend and a final flat road.

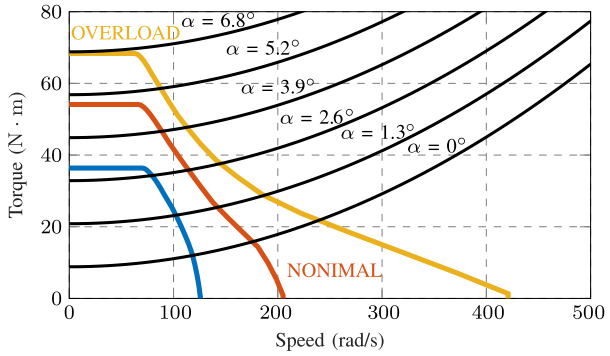

(a) Torque versus speed to the wheels.

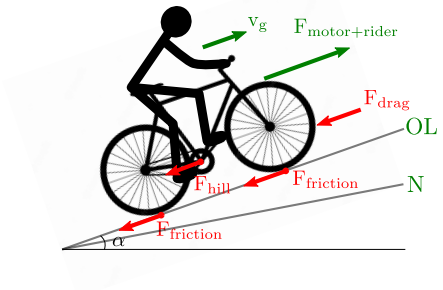

(b) Resistance to the motion.

Fig. 10: Slope overcoming capability of the motor.

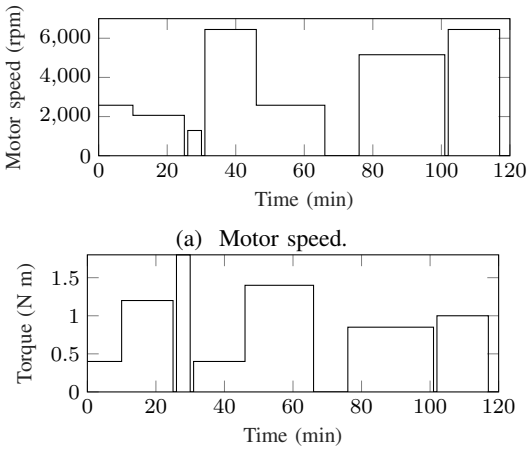

(a) Motor speed.

(b) Motor torque.

Fig. 11: Speed and torque requirements of the electric motor.

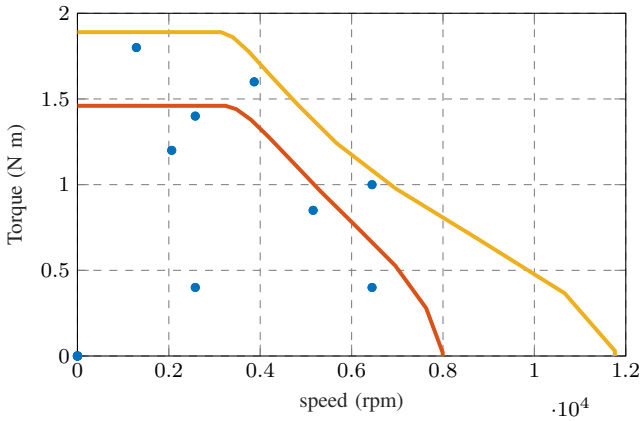

Fig. 12: Torque speed characteristic and drive cycle operating points.

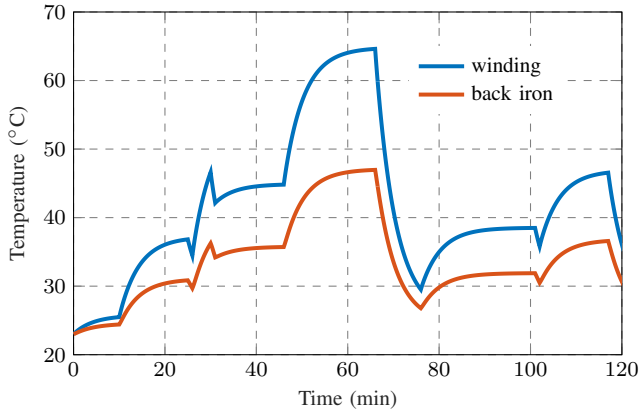

Fig. 13: Temperature evolution during the drive cycle.

Fig. 11a shows the electric motor speed requirement. It is worth noticing that it is limited to 25 km/h and it is equal to zero when the bicycle goes downhill. Fig. 11b shows the torque required from the electric motor to overcome hills or to reach a certain speed on a smooth terrain. It goes up to the maximum overload torque of the motor, when the trail effort increases. In Fig. 12 all operating points can be observed in the motor speed torque plane, already presented in the previous Section. It can be seen that most of the operating points lie within the nominal operating region. Only a few points are in the overload region, and they are all held for a time below the 4 min limit for thermal reasons.

Considering the torque and speed requirements, the current to supply can be obtained. Consequently, it is possible to esteem temperature evolution through the thermal network described previously. Fig. 12 shows the temperature evolution in time for the copper winding and the stator back-iron. The 13 different parts of the route are evident: the increasing temperature sections refer to the smooth or uphill terrain, while the downhill parts cause a temperature decrease. Starting from a 24 °C environmental temperature, the peak values reached are equal to 65 °C for the stator winding and 45 °C for the back-iron.

IV. Losses and Efficiency

This Section focuses on the computation of motor losses and the efficiency estimation. Magneto-static finite element simulations are carried out to evaluate Joule, iron and rotor losses.

A. Joule and iron losses

Losses during nominal and overload operation can be computed through the finite element simulation. Considering the current density J_{rms}, stator Joule losses are computed as:

$$P_{J,s} = J_{rms}^2 \cdot V_{Cu,s} \cdot \rho_{Cu,T} \tag{1}$$

where $\rho_{Cu,T}$ is the copper resistivity at the working temperature and $V_{Cu,s}$ is the volume of copper material in the stator.

Iron losses are computed by Steinmetz formulation, considering both hysteresis and eddy currents effects. Specific iron losses are computed considering the maximum flux density reached $\hat{B}$ and the specific frequency f, compared to the reference flux density $B_{fe}^* = 1.5$ T and frequency $f^* = 50$ Hz, respectively. Hysteresis accounts for 70 % of iron losses (coefficient $k_h = 0.7$), while eddy currents for 30 % of iron losses (coefficient $k_{ec} = 0.3$). Thus, specific iron losses are calculated as:

$$p_s = p_{s,fe}^* \cdot \left(\frac{\hat{B}}{B_{fe}^*}\right)^2 \cdot \left[k_h \cdot \left(\frac{f}{f^*}\right) + k_{ec} \cdot \left(\frac{f}{f^*}\right)^2\right] \tag{2}$$

where specific iron losses $p_{s,fe}^*$ depend on the iron lamination employed, in that case it is a Si-Fe 530-50 iron lamination. Considering iron weight G and an increase coefficient due to manufacturing k_m, iron losses are $P_{fe} = k_m \cdot p_s \cdot G$. Back-iron and teeth losses are computed separately ($P_{fe,bi}$ and $P_{fe,t}$, respectively), considering each region iron volume and the maximum flux density derived from FE simulation.

When the rated current is supplied, Joule losses are 35.9 W, while during overload they equal 63.8 W. Iron losses are similar, equal to about 9 W. This is due to the fact that flux-density on teeth and back-iron do not change a lot between rated and overload.

B. Rotor losses

Since e-bike electric motors usually run at high speeds, rotor losses are evaluated. They are caused by high frequency magnetic field generated at the air gap, that induces eddy currents in PMs. Such rotor losses increase the temperature rise of the rotor, which can cause severe overheating and PM irreversible demagnetization, and produce vibrations. Such losses can have a high impact on the motor efficiency when fractional-slot windings are employed. In fact, as observed in Fig. 3b for the $12/14$ configuration, the MMF generated by the stator winding is characterized by sub harmonics higher than the main harmonic. Since the sub harmonics have a wavelength higher than the corresponding wavelength of the main harmonic, their flux lines enter deeply in the rotor, causing higher induced currents.

In order to evaluate rotor losses, magneto-static simulations are carried out at different frequencies (depending on the harmonic order considered), following the procedure of [9], [10]. Fig. 14 shows the comparison of rotor losses during nominal and overload operation.

Rotor losses are 1.2 W during nominal operation and 1.4 during overload operation.

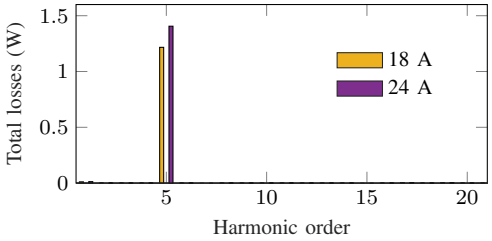

Fig. 14: Total losses due to MMF harmonics from the 1^{st} to the 21^{st} order, nominal and overload operation.

TABLE III: Motor performance under different loads, simulation results.

Parameter			Unit
Peak current	18	24	A
Current density	11	14.8	$\mathrm{A/mm^2}$
Torque	1.47	1.89	$\mathrm{N \cdot m}$
Torque ripple	2	2	%
Maximum power	290	390	W
Joule losses	35.9	63.8	W
Iron losses	8.9	8.9	W
Rotor losses	1.2	1.4	W
Efficiency	86.3	84	%
Temperature	75	110	°C
Maximum time	-	4	min

C. Total losses and efficiency

The total efficiency of the motor is esteemed considering only finite element simulation results. TABLE III shows the motor performance esteemed. It includes, rated torque, maximum power and maximum temperature reached. The efficiency is high during both nominal and overload operation. The overload efficiency is slightly lower due to the higher Joule losses, that are the main reason of the temperature rise. The overload operation allows delivering a 390 W mechanical power, but its operation is limited to maximum 4 minutes.

V. Conclusions

The study conducts a comprehensive analysis of a typical electric motor configuration used in e-bikes. A thorough examination of the motor's performance under different operating conditions is presented, considering both finite element simulations and experimental testing. Simulation results correspond to experimental tests, describing the operation of a typical e-bike motor under both nominal and overload conditions. A thermal test allows identifying the nominal and overload current of the motor. The maximum current can be sustained by the motor for a maximum time of 4 min, due to overheating. The torque increases almost linearly with the current supplied, while the ripple is always low. Maximum torque (and power) versus speed characteristics are computed, showing that the maximum speed achievable is 16000 rpm during overload operation. Computing resistance forces on the bicycle-rider system and considering the gear ratio of the machine, the maximum tilt that can be overcame can be esteemed. The rider-bicycle system can overcome a tilt of 2.8 degrees (5 %

slope) during nominal operation, 6.4 degrees (11 % slope) during overload operation, without any muscular contribution. Considering finite element simulation results, the efficiency equals to 86 % during nominal operation, while it is slightly reduced to 84 % during overload.

REFERENCES

[1] A. Muetze and Y. C. Tan, "Electric bicycles - a performance evaluation," *IEEE Industry Applications Magazine*, vol. 13, no. 4, pp. 12–21, 2007.

[2] T. Chan, L.-T. Yan, and S.-Y. Fang, "In-wheel permanent-magnet brushless DC motor drive for an electric bicycle," *IEEE Transactions on Energy conversion*, vol. 17, no. 2, pp. 229–233, 2002.

[3] R. Nasiri-Zarandi, A. Karami-Shahnani, M. S. Toulabi, and A. Tessarolo, "Design and experimental performance assessment of an outer rotor pm-assisted synrm for the electric bike propulsion," *IEEE Transactions on Transportation Electrification*, vol. 9, no. 1, pp. 727–736, 2023.

[4] S. Koyuncu, U. Tuncer, A. Dalcali, and S. Oncu, "External rotor 6/8 switched reluctance motor design for e-bike," in *2021 10th International Conference on Renewable Energy Research and Application (ICRERA)*, 2021, pp. 131–135.

[5] B. Howey, B. Bilgin, and A. Emadi, "Design of an external-rotor direct drive e-bike switched reluctance motor," *IEEE Transactions on Vehicular Technology*, vol. 69, no. 3, pp. 2552–2562, 2020.

[6] X. Fan, B. Zhang, R. Qu, D. Li, J. Li, and Y. Huo, "Comparative thermal analysis of IPMSMs with integral-slot distributed-winding (ISDW) and fractional-slot concentrated-winding (FSCW) for electric vehicle application," *IEEE Transactions on Industry Applications*, vol. 55, no. 4, pp. 3577–3588, 2019.

[7] D. Meeker. Finite element method magnetics. [Online]. Available: https://www.femm.info/wiki/HomePage

[8] M. Corno, P. Spagnol, and S. M. Savaresi, "Road slope estimation in bicycles without torque measurements," *IFAC Proceedings Volumes*, vol. 47, no. 3, pp. 6295–6300, 2014.

[9] N. Bianchi, S. Bolognani, and E. Fomasiero, "A general approach to determine the rotor losses in three-phase fractional-slot pm machines," in *2007 IEEE International Electric Machines and Drives Conference*, vol. 1, 2007, pp. 634–641.

[10] N. Bianchi, S. Bolognani, and E. Fornasiero, "An overview of rotor losses determination in three-phase fractional-slot pm machines," *IEEE Transactions on Industry Applications*, vol. 46, no. 6, pp. 2338–2345, 2010.